Surface Lattice Resonances in Self-Assembled Gold Nanoparticle Arrays: Impact of Lattice Period, Structural Disorder, and Refractive Index on Resonance Quality

Ekaterina Ponomareva,[†] Kirsten Volk,[†] Paul Mulvaney,[‡] and Matthias Karg[*,†]

[†]*Institut für Physikalische Chemie I: Kolloide und Nanooptik, Heinrich-Heine-Universität Düsseldorf, Universitätsstraße 1, D-40225 Düsseldorf, Germany*

[‡]*ARC Centre of Excellence in Exciton Science, The University of Melbourne, School of Chemistry, Parkville, VIC 3110, Australia*

E-mail: karg@hhu.de

Abstract

Surface lattice resonances are optical resonances comprised of hybridized plasmonic and diffractive modes. These collective resonances occur in periodic arrays of plasmonic nanoparticles with wavelength-scale interparticle distances. The appearance and strength of surface lattice resonances strongly depend on the single particle localized surface plasmon resonance and its spectral overlap with the diffractive modes of the array. Coupling to in-plane orders of diffraction is also strongly affected by the refractive index environment and its symmetry.

In this work, we address the impact of the interparticle distance, the symmetry of the refractive index environment and structural imperfections in self-assembled colloidal monolayers on the plasmonic-diffractive coupling. For this purpose we prepared hexagonally ordered, non-close packed monolayers of gold nanoparticles using a fast and efficient, interface-mediated, colloidal self-assembly approach. By tuning the thickness and deformability of the polymer shells, we were able to prepare monolayers with a broad range of interparticle distances. The optical properties of the samples were

studied experimentally by UV-Vis spectroscopy and theoretically by Finite Difference Time Domain (FDTD) simulations. The measured and simulated spectra allow a comprehensive analysis of the details of electromagnetic coupling in periodic plasmonic arrays. In particular we identify relevant criteria for surface lattice resonances in the visible wavelength range with optimized quality factors in self-assembled monolayers.

Introduction

Metal nanostructures are known to interact with external electromagnetic fields due to the excitation of surface plasmon modes - collective oscillations of the conduction electrons.[1] The strength and energy as well as the number of these modes depend critically on the type of metal,[2] the nanostructure size[3,4] and shape,[3,5,6] the dielectric properties of the surrounding environment[3,7] and the nanostructure arrangement.[8–13] Individual nanoparticles composed of gold or silver with diameters smaller than approximately 100 nm primarily support single localized surface plasmon resonances (LSPRs) that are due to dipolar excitations of the conduction electrons.[4,14] These dipolar LSPRs can be excited with light in the visible wavelength range and this phenomenon explains the vivid colours of dilute dispersions of gold and silver nanoparticles.[15,16] While for the smallest sizes, up to a few tens of nanometres in diameter, the interaction with light is dominated by absorption, scattering becomes dominant for larger sizes because (Rayleigh) scattering intensity scales with the sixth power of the particle diameter ($I_{sc} \propto D^6$). LSPRs concentrate electromagnetic fields into nanoscale volumes and exhibit extinction cross-sections exceeding those of molecular absorbers such as organic dyes by several orders of magnitude and consequently, they may have applications in solar energy harvesting,[17,18] ultrasensitive sensing,[19] lasing[20] and photocatalysis.[21] Nevertheless, gold in particular is a relatively poor plasmonic material and suffers high intrinsic absorption losses.[22,23] The Full Width at Half Maximum (FWHM) of the LSPR is approximately 80 to 100 nm for gold nanoparticles in the size range of $\sim$ 8 to 100 nm.[24,25] The strong damping and the resulting low quality factors ($Q = \lambda/\Delta\lambda$) limit the potential of

gold nanoparticles for many nanophotonic applications. Consequently strategies are needed to enhance the Q-factor; ideally these strategies should employ both simple building blocks and scalable fabrication procedures. A powerful strategy for reducing losses in noble metal nanostructures is to arrange the nanoparticles into periodic arrays with wavelength-scale periodicities. Short- and long-range interactions in such arrays can result in higher field enhancements and resonances with significantly improved Q-factors.[26,27] For large enough periodicities, surface lattice resonances (SLRs) result from the collective radiative coupling between the single particle LSPRs and the in-plane modes of diffraction, i.e. the grating Rayleigh Anomaly (RA).[24,28] This form of diffractive-plasmonic coupling requires a uniform dielectric environment surrounding the plasmonic particle array. SLRs were first observed and described in 2008 by Kravets *et al.*[29] and by Auguié and Barnes.[30] Since then the fundamental spectroscopy of SLRs and the experimental realization of periodic plasmonic arrays that can support high Q-factor SLRs have both become topics of intense study, as reflected by the appearance of several recent reviews.[9,24,31]

Until now, electron-beam lithography has been the method of choice for producing periodic particle arrays with nearly perfect structural control. Using this method arrays with different lattice symmetries[32] and even arrays comprising asymmetric particle dimers[33] have been prepared. However, more recently methods suitable for large area fabrication such as soft interference lithography have gained increasing interest.[34] As an alternative, our group has demonstrated that colloidal self-assembly of core-shell building blocks is well-suited to the production of periodic plasmonic particles arrays which can extend over cm^2 areas.[35–37] We have also shown that such arrays can support the formation of SLRs, albeit possessing relatively low Q-factors.[38,39] While self-assembly offers rapid, low-cost and low-tech production of large area arrays from relatively simple building blocks,[10] the method typically results in significantly more defects and smaller domain sizes. Hence, it is important to identify experimental parameters that can yield high quality resonances. For domain sizes much larger than the exciting wavelength, a larger lattice period will result in a higher quality

mode;[30,40] however different rules may apply to self-assembled lattices with limited domain size and multidomain character. A direct comparison between experimental and theoretical extinction properties of imperfect periodic particle arrays as a function of the lattice period is currently not available. Consequently it remains unclear how competitive self-assembly strategies are compared to other techniques used for the fabrication of particle arrays that support SLRs.

In this work, we investigate the optical properties of periodic plasmonic monolayers in both symmetric and asymmetric refractive index environments. We prepare these monolayers by a readily available, robust and efficient interface-mediated self-assembly procedure that yields hexagonally ordered particle arrangements on cm^2 substrates. By using colloidal building blocks with plasmonic gold nanoparticle cores and soft, deformable polymer shells of different thicknesses, we obtain lattices with a broad range of interparticle distances. This allows us to study the optical response of the periodic structures and the effects of spectral overlap between the single particle LSPRs and the in-plane modes of diffraction. Different electromagnetic coupling scenarios are identified including long-range (radiative) coupling to grating RAs. We study the effects of limited domain size, scattering losses at domain boundaries and other structural imperfections. Our findings enable the Q-factor of surface lattice resonances in self-assembled periodic plasmonic monolayers to be optimized.

Experimental Section

Chemicals

Gold(III)chloride trihydrate ($HAuCl_4$; Sigma-Aldrich, ≥99.999 %), sodium citrate dihydrate (Sigma-Aldrich, ≥99 %), sodium dodecyl sulfate (SDS; Sigma-Aldrich, p.a.), butenylamine hydrochloride (BA; Sigma-Aldrich, 97 %), *N*-isopropylacrylamide (NIPAM; TCI, >98.0 %), *N,N'*-methylenebisacrylamide (BIS; Sigma-Aldrich, ≥99 %), potassium peroxodisulfate

(PPS; Sigma-Aldrich, ≥99 %), cetyltrimethylammonium chloride (CTAC; Sigma-Aldrich, 25 wt%, H_2O), ascorbic acid (Roth, p.a.), ethanol (Honeywell, p. a.) and 1,4-dioxane (p.a., Fisher Chemicals) were used as received. Milli-Q water (Millipore, $R > 18\ M\Omega cm$) was used for all syntheses, purifications and self-assembly steps.

Synthesis

Core-shell particles with gold cores and soft hydrogel shells (Au-PNIPAM) were synthesized in different steps. First, spherical, citrate-stabilized gold nanoparticles (Au-NPs) of approximately 15 nm in diameter were synthesized according to the Turkevich protocol.[41] Afterwards seeded precipitation polymerization of NIPAM and the cross-linker BIS using the Au-NPs as seed particles was performed following the protocol by Rauh *et al.*[42] Using three different NIPAM feed concentrations and fixed cross-linker contents (15 mol% referred to NIPAM) we prepared core-shell particles with different shell sizes (see table 1). Finally the gold cores of all Au-PNIPAM batches were stepwise overgrown with gold to reach approximately 100 nm in diameter. The overgrowth protocol was adapted from Honold *et al.*[35] For the sake of clarity, the different core-shell samples are labelled Au-PNIPAM$_{336}$, Au-PNIPAM$_{354}$ and Au-PNIPAM$_{367}$ with the numbers in subscripts corresponding to the hydrodynamic radius of the core-shell particles measured at 25° C. The final particles were purified by centrifugation and redispersion of the residues in water. Centrifugation and redispersion were repeated three times at 5200 rcf (relative centrifugal force) for 30 minutes each. After the last centrifugation, the entire batch particles was redispersed in 150 μl ethanol. A detailed description of the synthesis steps, as well as exemplary TEM images and UV-Vis absorbance spectra from each synthesis step (Figure S1), can be found in the Supporting Information.

Table 1: Concentration, c, and masses, m, of the monomer (NIPAM) and cross-linker (BIS) used for the seeded precipitation polymerization. The reaction volumes were 100 ml for each synthesis. Hydrodynamic diameter, d_h, of the core-shell particles from dynamic light scattering measured in dilute aqueous dispersion in the swollen state of the shell (25° C).

Sample	c(NIPAM) [M]	m(NIPAM) [g]	m(BIS) [g]	d_h [nm]
Au-PNIPAM$_{336}$	0.052	0.587	0.134	336
Au-PNIPAM$_{354}$	0.058	0.656	0.134	354
Au-PNIPAM$_{367}$	0.084	0.946	0.194	367

Fabrication of periodic particle arrays

The fabrication of hexagonally ordered Au-PNIPAM particle arrays on glass substrates was carried out by following the protocol of Volk et al.[38] Briefly, a small crystallization dish was filled with Milli-Q water and 7 μl of the particle dispersion (purified, in ethanol) were gently transferred to the air/water interface. At the interface the particles spontaneously self-assembled into a freely floating monolayer. Floating monolayers were transferred onto glass substrates by immersing the substrate fully into the bulk water phase below the monolayer and then withdrawing the substrate slowly through the monolayer. Thereby the monolayer was collected onto the glass. Immediately after withdrawal of the substrates, the samples were dried using a heat-gun to blow warm air onto the back of the glass. A video demonstrating the self-assembly process can be found in the Supporting Information. To achieve the homogeneous refractive index environment required for radiative coupling to in-plane modes of diffraction, the monolayer samples were coated in a PNIPAM layer by spin-coating linear PNIPAM (65000 g/mol, synthesized according to Ebeling and Vana[43]). Spin-coating was performed by applying 60 μl of a 1,4-dioxane solution containing the polymer (100 mg PNIPAM in 2 ml dioxane) and then applying 2000 rpm for 90 s. Under these conditions the resulting PNIPAM films had thicknesses of approximately 300 nm.

Methods

Transmission electron microscopy:

A Zeiss CEM902 transmission electron microscope (TEM) was used for the determination of particle size, size dispersity and structure. TEM measurements were performed at an acceleration voltage of 80 kV in bright-field operation. For each sample, a drop of a dilute aqueous particle dispersion was placed on carbon-coated copper grids and left to dry in air. Statistical analysis of the core sizes was carried out by measuring 200 particles from various TEM images using the ImageJ software.[44]

Atomic force microscopy:

Atomic force microscopy (AFM) topographic images (10 × 10 μm^2) were recorded with a Nanowizard 4 (JPK Instruments) in intermittent contact mode against air. OTESPA-R3 AFM probes (Bruker) were employed for image recording. The cantilevers possess a resonance frequency of approximately 300 kHz and a spring constant of approximately 26 N/m. The tip geometry was a visible apex with a nominal tip radius of 7 nm.

UV-Vis Spectroscopy:

Extinction spectra were recorded with a Specord S 600 UV-vis spectrophotometer (Analytik Jena AG) in transmission geometry. Spectra of the particle dispersions were measured in 1 × 1 cm^2 PMMA cuvettes. Particle monolayers on glass substrates were positioned upright in the light path using a solid sample holder. All extinction spectra were corrected for background using either a cuvette with water or an empty glass substrate.

Dark-field microscopy:

The optical microscopy images were captured in dark-field mode with reflection configuration using a Nikon ECLIPSE LV100D-U microscope equipped with a halogen lamp (12 V, 50 W), a dark-field condenser and a CMOS camera (Thorlabs, DCC1645c-HQ). There are three lenses equipped on the microscope, Nikon LU Plan Fluor 20x/0.45, Nikon LU Plan ELWD 50x/0.55, and Nikon Lu Plan Fluor 100xA/0.9. Local scattering spectra were recorded with a CCD camera (Princeton Instruments, Pixis 1024F) and an imaging spectrograph (Princeton Instruments, Acton MicroSpec 2150i).

FDTD simulations:

Extinction spectra and E-field maps were calculated using the FDTD method with commercial software from Lumerical Solutions, Inc. (FDTD Solutions, Version 8.18.1332). For the finite size lattices, absorption and scattering spectra were simulated in a box with a perfectly matched layer (PML) boundary conditions in the x-, y-directions (layer direction) and the z-direction. Unless otherwise specified the finite size lattices consist of 61 particles which correspond to a domain size of four. We utilized a Total-Field Scattered-Field (TFSF) source and a box of power monitors consisting of the total field and scattered field monitors. For the infinite lattices and electromagnetic field simulations periodic boundary conditions (PBC) in both the x- and y-directions (layer direction) and a perfectly matched layer in the z-direction (beam direction) were used. A linear polarized plane wave source with excitation along the z-axis was injected. A transmission monitor was located at both ends of the FDTD simulation box in the beam direction. Following settings were kept the same for all simulations. Particle sizes and distances were used as obtained from the experiments. The wavelength dependent RI of the gold core was taken from literature.[45] For the glass substrates a constant RI of 1.52 was used and for the air background 1. The PNIPAM film was simulated with 300 nm thickness and a constant RI of 1.49[46] slightly smaller than 1.52[47] to account for a small amount of residual water. The auto shut-off was set at 10^{-5}.

Results and discussion

Au-PNIPAM particle characterization

Core-shell colloids with plasmonic gold cores and three thicknesses of soft PNIPAM hydrogel shells were synthesized. A schematic representation of the particles is shown in figure 1 a). We aimed at synthesizing particles that feature nearly the same core diameter, d_{core}, so that the plasmonic properties, i.e. the position and intensity of the LSPR, are comparable despite the different thicknesses of the dielectric PNIPAM shells. Figure 1 b) shows normalized absorbance spectra recorded from dilute aqueous dispersions of the Au-PNIPAM particles.

All samples feature a single LSPR peak attributed to a dipolar mode. The LSPR positions are λ_{LSPR} = 577 nm for Au-PNIPAM$_{336}$, λ_{LSPR} = 582 nm for Au-PNIPAM$_{354}$ and λ_{LSPR} = 583 nm for Au-PNIPAM$_{367}$, thus matching closely. Due to the relatively large linewidths (FWHM $\approx$ 137 nm) all particles possess low Q-factors of $Q \approx 4$. Figures 1 c), d) and e) show TEM images of the different particles. In all three images, the core-shell structure is clearly visible due to the pronounced contrast difference between the high electron density gold cores and the low electron density PNIPAM shells. The shells are imaged in their dried and collapsed state because of the measuring conditions during TEM imaging. Thus the shells appear thinner than in their swollen state in aqueous dispersion. Dynamic light scattering from dilute dispersions measured at 25 ° C (swollen state) revealed hydrodynamic diameters of d_h = 336 nm, d_h =354 nm, and d_h = 367 nm, respectively. The average core sizes, d_{core}, were determined directly from TEM images. The cores of the three core-shell systems have nearly the same size (d_{core} = 99 $\pm$ 8 nm (Au-PNIPAM$_{336}$), d_{core} = 102 $\pm$ 8 nm (Au-PNIPAM$_{354}$) and d_{core} = 96 $\pm$ 9 nm (Au-PNIPAM$_{367}$)). The corresponding size distributions are shown in figures 1 f), g) and h). The standard deviations of the average diameter are 8-9 %, emphasizing the good control of our overgrowth procedure (see Experimental Section and Supporting Information for more details). A further reduction in the polydispersity of the core sizes might be achievable by further optimization of the synthesis protocol but this is not expected to cause any significant increase in the Q-factor of the LSPR. Indeed, a further increase in core diameter will eventually lead to broader linewidths and thus reduced Q values due to the appearance of quadrupolar modes and retardation of the dipolar mode.[25]

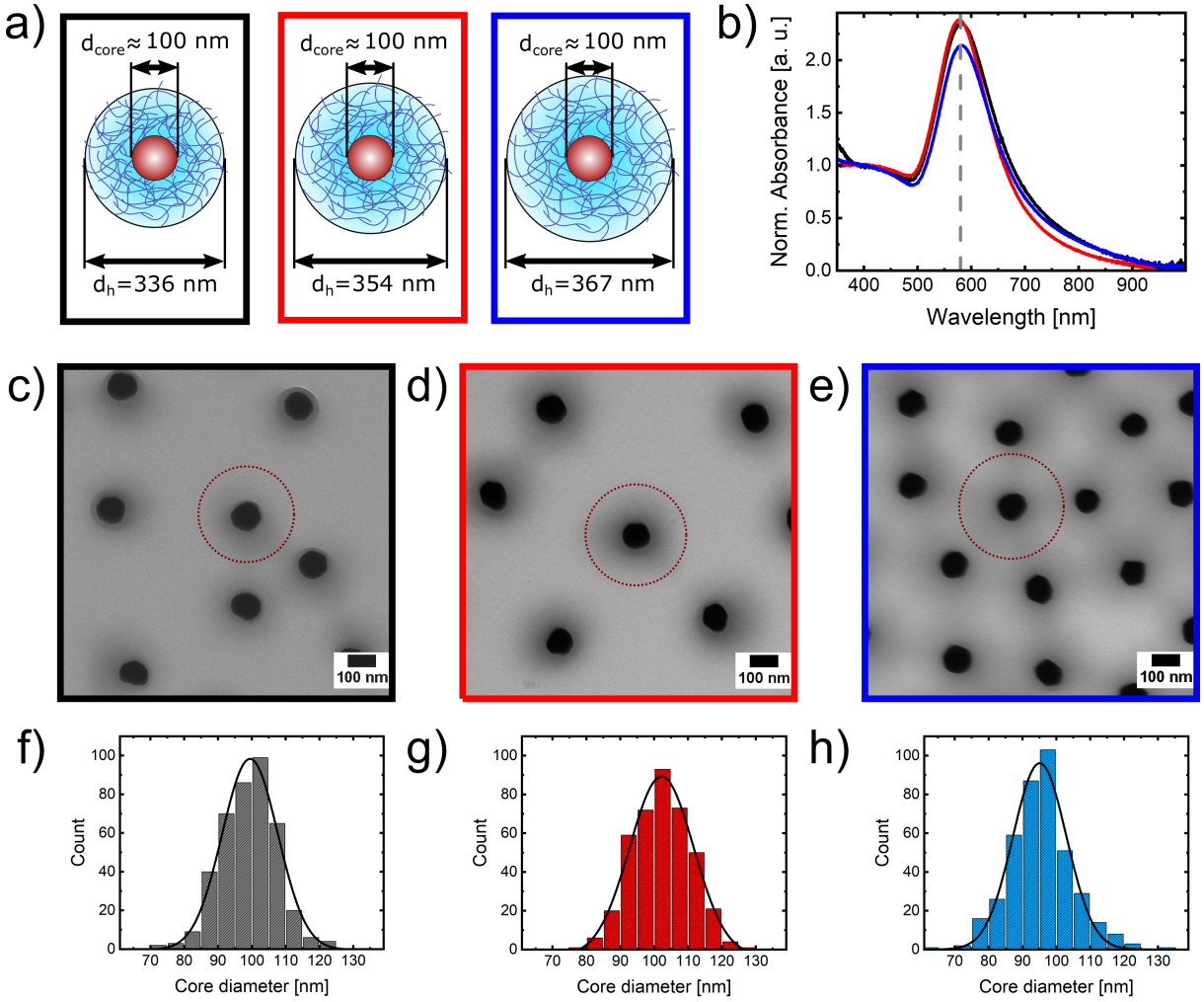

Figure 1: Au-PNIPAM building blocks for monolayer preparation, Au-PNIPAM$_{336}$ in black, Au-PNIPAM$_{354}$ in red and Au-PNIPAM$_{367}$ in blue. a) Schematic representation of the core-shell structure of the Au-PNIPAM particles with d_{core} indicating the core diameter and d_h corresponding to the hydrodynamic diameter. b) Absorbance spectra normalized to the absorbance at 400 nm. The dashed grey line highlights the LSPR position, λ_{LSPR}. c), d) and e) Representative TEM images for each batch of particles. The red dotted circles indicate the corresponding hydrodynamic size determined from DLS. f), g) and h) Histograms for the core diameters determined from TEM images.

Monolayers from Au-PNIPAM particles

We used the different Au-PNIPAM core-shell particles to prepare hexagonally ordered monolayers with a broad range of nearest-neighbour centre-to-centre interparticle distances, d_{c-c}, by an interface-mediated self-assembly approach.[38] Control of d_{c-c} was realized 1) by us-

ing different shell thicknesses and 2) by using sequential transfer from floating monolayers at the air/water interface where the packing fraction is reduced after every withdrawal of a monolayer sample. A densely packed monolayer is firstly prepared at the interface. In this case, the value of d_{c-c} is close to the bulk hydrodynamic diameter of the particles.[36] Then a fraction of the monolayer is removed from the interface by transfer onto the first substrate, resulting in an expansion of the remaining monolayer driven by interfacial tension and the deformability of the PNIPAM shells. Now withdrawal of some of this monolayer onto another substrate yields a sample with a slightly reduced particle density, and d_{c-c} is increased by about 1.02 up to 1.1. Using this multistep transfer process in combination with particles having a range of different shell thicknesses, allows the fabrication of monolayers with various values of d_{c-c}. In this work d_{c-c} was varied between 342 and 448 nm using the Au-PNIPAM$_{336}$ particles, between 448 and 500 nm using the Au-PNIPAM$_{354}$ particles and between 500 and 573 nm with the Au-PNIPAM$_{367}$ particles. A video of the assembly approach is provided in the Supporting Information where changes in the monolayer density become clearly visible because the reflected colour changes due to the changing particle spacing. Since the spacing in the monolayers is only determined by the dielectric PNIPAM shells and because the sizes and thus LSPR properties of the cores are nearly identical, the only optically relevant parameter that is altered between the samples is the lattice spacing.

Figures 2 a) and d) show photographs of the light reflection from particle arrays with different lattice spacing on glass substrates illuminated by a white light source from the side. In both cases the monolayers cover the full, macroscopic substrates as evident from the opalescent colours. Additionally, images of the same samples were taken using a dark-field microscope (DFM) at different magnifications. At 20 $\times$ magnification (Figures 2 b) and e)), the two samples show clear differences in colour. The sample with $d_{c-c} = 458 \pm 29\ nm$ b) appears orange, while the sample with the larger lattice spacing ($d_{c-c} = 567 \pm 32\ nm$) appears green. The observed colours are a combination of the scattering from the individual particles

and the Bragg diffraction. The latter depends strongly on the distance between the particles, the light incident and the detection angle. At 100 × magnification, both samples appear similar in colour, yellowish-orange caused by the scattering of individual gold particles. Due to the larger aperture of the objective, the diffraction of the lattices cannot be observed. The DFM images confirm the homogeneity of the samples on different length scales. Furthermore the images taken at the highest magnification allow for identification of particle positions at the single particle level. The DFM images recorded at 100 × magnifications are also shown in the Supporting Information with larger image sizes (see Figure S2). Using the particle positions, we calculated the Fast Fourier Transformations (FFTs) that are shown as insets in Figures 2 c) and f). Both FFTs show Bragg peaks with hexagonal symmetry and at least three orders, reflecting the high degree of hexagonal ordering. Additionally, monolayers with different values of d_{c-c} were characterized using AFM and representative images are shown in Figure S3 (Supporting Information). These images and the respective FFTs of the particle positions confirm the hexagonal ordering of the samples. Furthermore, pair correlation functions g(r) were calculated allowing for the quantitative analysis of the degree of order. For all selected samples, g(r) shows at least 6-7 clearly distinguishable peaks indicating large crystalline domain sizes. Throughout this manuscript, the values of d_{c-c} have been calculated from the first maximum of g(r) which has in turn been determined from a Lorentz fit to the function.

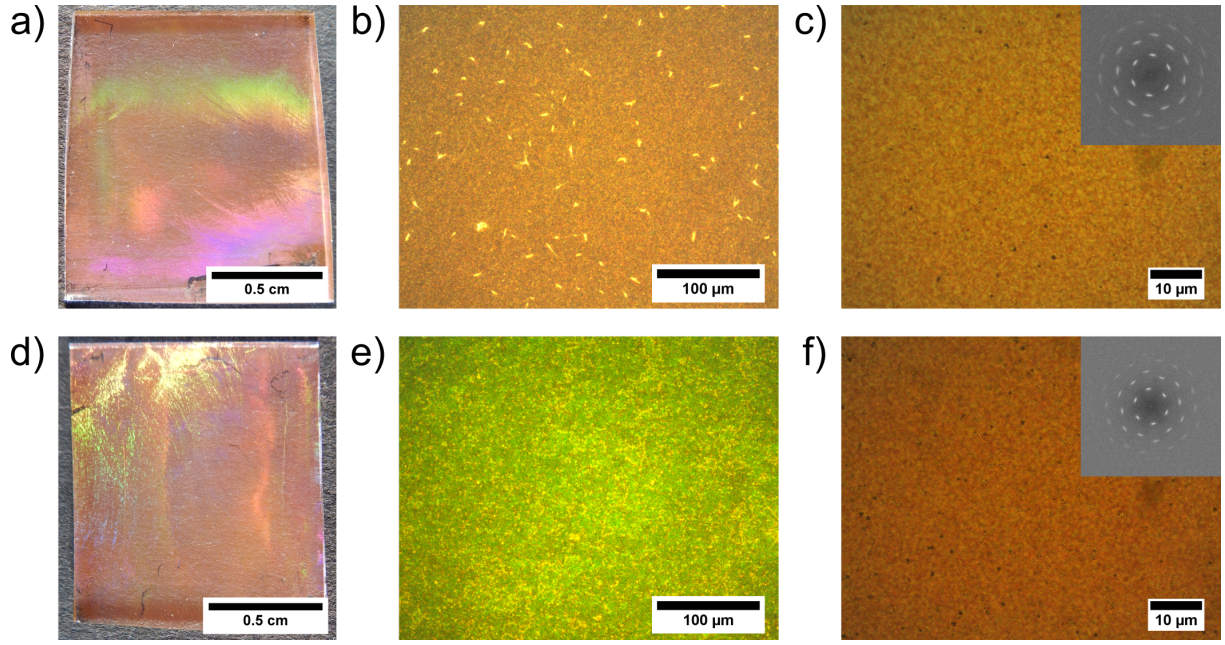

Figure 2: Monolayer characterization at different magnifications. Top row: Monolayer with $d_{c-c} = 458 \pm 29\ nm$. Bottom row: $d_{c-c} = 567 \pm 32\ nm$. a) and d) Digital photographs of the samples. b) and e) DFM images with 20 × magnification. c) and f) DFM images with 100 × magnification. The insets show FFTs calculated from the DFM images.

Since the resolution of the DFM image in Figure 2 f) is sufficient to track the positions of the large majority of the particles at the single particle level, we can use this image to analyze the crystalline domains. Therefore, we have used a triangulation analysis introduced by Hillebrand *et al.*[48] Figure 3 shows the DFM image with the detected single crystalline domains (hexagonal order) highlighted in different colours. Particles without hexagonal coordination are highlighted in white. At first glance, we see that the majority of the particles have hexagonal coordination and thus are assigned to crystalline domains. The image contains a rather large number of domains of various sizes. The largest domain contains more than 5,000 particles. Furthermore, we are able to identify 16 domains that contain 100 or more particles. In order to analyze the domain sizes of monolayers with smaller lattice constants, we have recorded height profiles by AFM. Figure S4 a) in the Supporting Information shows 40×40 μm^2 scans of monolayer samples with values of $d_{c-c}s$ of 375, 458 and 567 nm. From the domain analysis in Figures S4 b) and c) we find 1) that

much larger, single crystalline domains are detected as compared to the previously discussed DFM image and 2) that the domain size seems to increase with increasing d_{c-c}. We can certainly conclude that the degree of order does not decrease with increasing d_{c-c}. This will become relevant when discussing diffractive-plasmonic coupling later on. The fact that larger domains are found from analysis of the AFM images is simply related to the better spatial resolution in AFM. Thus AFM allows much more precise determination of the central x-,y-positions of individual particles.

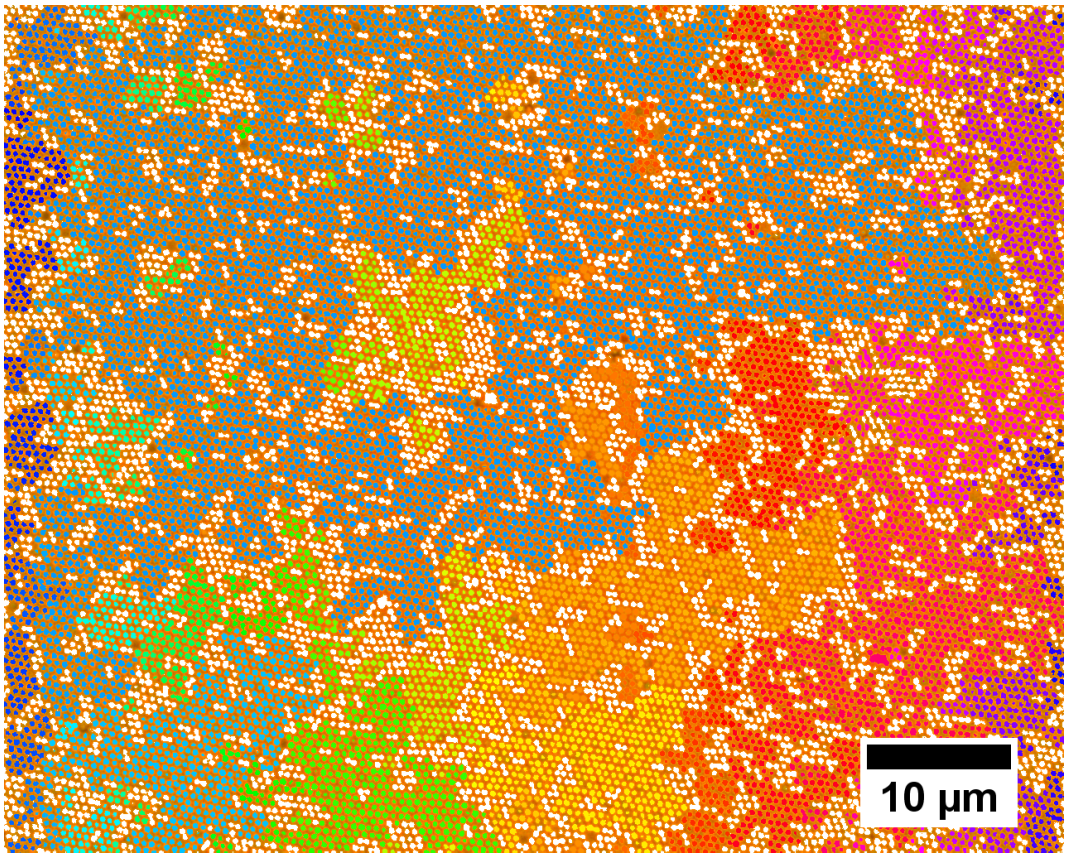

Figure 3: Analysis of crystalline domains. a) DFM image with $d_{c-c} = 567 \pm 32$ nm. Different crystalline domains are highlighted in different colours. Particles without hexagonal coordination are coloured in white.

Optical properties in an asymmetric RI environment

In the following we will address the dependence of the optical properties of our periodic particle arrays on the interparticle spacing, d_{c-c}. We start by considering arrays where there

is a glass substrate (RI = 1.52) and air (RI = 1.00) is the superstrate. A schematic depiction of the sample geometry is shown in figure 4 a). Figure 4 b) summarizes absorbance spectra of selected samples measured in normal transmission. Spectra from a larger set of monolayers can be found in the Supporting Information (Figure S5 a)). All of these arrays exhibit a single resonance peak whose resonance position, width, and intensity depends on the lattice spacing. With decreasing d_{c-c}, the resonance shifts to smaller wavelengths, becomes more intense and the FWHM decreases. The increase in resonance intensity is primarily attributed to the increasing particle density (Beer-Lambert law) as the lattice spacing is reduced. For the largest spacing, where $d_{c-c} = 573$ nm, we find a resonance position $\lambda_{max} = 595$ nm and a FWHM of 145 nm. Both values are close to the ones obtained from measurements in dilute aqueous dispersions (RI = 1.33) with $\lambda_{max} \approx 580$ nm and a FWHM of 137 nm. The slight redshift of the monolayer sample is related to the small increase in the effective RI for the combination of glass substrate with air superstrate. There is also a small increase in the effective RI due to the collapsed PNIPAM shell surrounding each gold core. We have also measured the spectrum of a monolayer sample on glass with a random particle distribution and a very small packing fraction (see Figure S6).This yields a resonance at $\lambda_{max} = 595$ nm perfectly matching the resonance of the ordered monolayer sample with $d_{c-c} = 573$ nm. This confirms that electromagnetic coupling is absent for large lattice spacings and the observed resonance shifts compared to particles in solution are due to changes in the RI environment. If we now look at the monolayer sample with the smallest lattice spacing ($d_{c-c} = 342$ nm), the resonance peak appears at $\lambda_{max} = 561$ nm, i.e. it is significantly blueshifted compared to the LSPR observed in dilute particle dispersions. Furthermore the FWHM is reduced to 78 nm. Both the blueshift and the reduction in linewidth are attributed to long-range radiative interactions between the gold nanoparticle dipoles.[49,50] At these still relatively large interparticle distances, we can exclude near-field electromagnetic coupling. This only becomes significant for interparticle spacings smaller than 2.5 times the particle diameter in the case of gold.[51]

In order to support our experimental findings we have also performed FDTD simulations. Calculated spectra are shown in figure 4 c). The observed peak positions, widths and intensities nicely match our experimental results as is seen from a direct comparison of the corresponding values summarized in table 2.

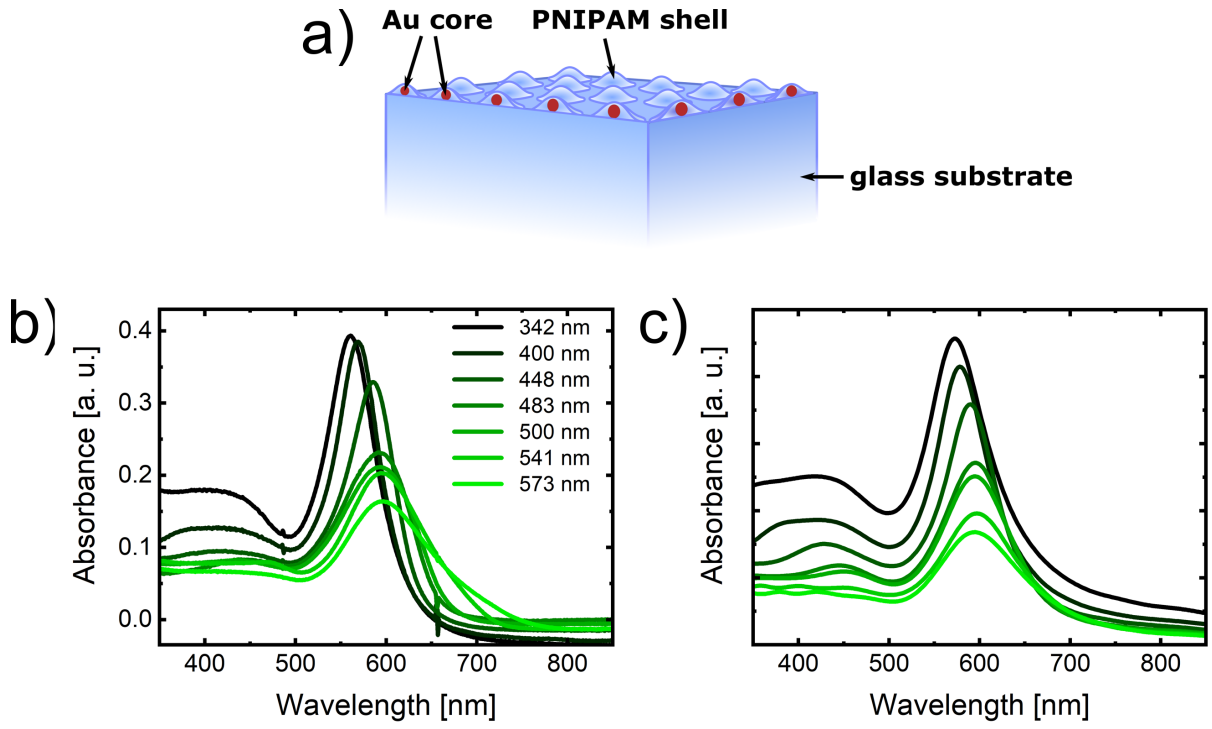

Figure 4: Optical properties of particle arrays in an asymmetric RI environment. a) Schematic depiction of the periodic particle array on a glass substrate with air as superstrate. b) Experimental absorbance spectra measured from samples with values of d_{c-c} ranging from 342 nm to 573 nm. c) Corresponding theoretical spectra from FDTD simulations of finite lattices (domain size 4) using the experimental values of d_{c-c} from b). The same colour code was used as in b).

Optical properties in a symmetric RI environments

In order to enhance radiative electromagnetic coupling, we need a higher RI superstrate which closely matches the RI of the glass substrate. To achieve this, we have deposited 300 nm thick polymer coatings on top of the particle arrays. This thickness is sufficient to enable observation of diffractive-plasmonic coupling.[39] A schematic depiction of the sample geome-

try is shown in figure 5 a). Note that, first of all, we need to determine the uncoupled single particle resonance as a reference. Figure 5 b) shows the simulated, single particle spectrum for a Au-PNIPAM particle on a glass substrate with a 300 nm thick topcoating of PNIPAM (RI = 1.49). We predict an LSPR at λ_{LSPR} = 604 nm, highlighted by the vertical grey dashed line. As a consequence of the higher RI superstrate, the LSPR position is shifted to the red (by approximately 9 nm). The coloured vertical lines in Figure 5 b) correspond to the calculated spectral positions of the $\{1, 0\}$ diffraction modes for the hexagonally ordered monolayers with varying d_{c-c}. The calculation is explained in the Supporting Information.

Figure 5 c) shows experimental absorbance spectra for selected monolayer samples immersed in symmetric RI environments. Spectra from a larger set of monolayers can be found in the Supporting Information (Figure S5 b)). To allow for a better comparison of the resonance intensities, the spectra in Figure 5 c) have been normalized to the same particle density (10 particles per μm^2). Looking at the smallest values of d_{c-c} (342 and 400 nm) where the diffractive modes are significantly blue-shifted compared to the single particle LSPR (Figure 5 b), we observe single resonance peaks. Here the sample with d_{c-c} = 400 nm features a resonance that is more intense, red-shifted and with a reduced linewidth compared to d_{c-c} = 342 nm. As in the case of asymmetric RI environments, we attribute these spectral differences to long-range radiative interactions between the dipoles. At d_{c-c} = 448 nm the strongest resonance appears at 638 nm with an even higher intensity and reduced linewidth. For this sample the $\{1, 0\}$ diffraction modes and the single particle LSPR overlap strongly and diffractive-plasmonic coupling is enabled, resulting in a true SLR. Although the RI of the PNIPAM superstrate (RI = 1.49) and the glass substrate (RI = 1.52) are not perfectly matched, an SLR is supported. This finding is in agreement with the work of Yang et al. who showed that SLRs are tolerant of RI mismatches up to $\Delta RI \sim 0.05$.[52] In addition the spectrum features a weak shoulder at approximately 530 nm. This mode is attributed to a weak plasmonic contribution.[53] With further increases in d_{c-c}, the SLRs shift to the red

and become broader and weaker. At the same time the plasmonic contribution at shorter wavelengths becomes more pronounced. For the sample with the largest spacing (d_{c-c} = 573 nm), where the $\{1, 0\}$ diffraction modes appear in the long wavelength tail of the single particle LSPR, the plasmonic contribution almost resembles the uncoupled LSPR response of the component building blocks and only a weak and broad SLR at 726 nm is observed. The increase in linewidth of the SLR with increasing d_{c-c} indicates a decrease in the coupling strength. While for a perfect particle lattice with an effectively infinite particle number, a reduction of the SLR linewidth is expected for increasing lattice constants, we clearly observe the opposite effect.

We explain this in terms of the finite size of the single crystalline domains in our monolayers as discussed in the previous section. Our explanation is supported by the work of Zou et al.[54] The authors studied the optical response of a two-dimensional array of 400 nanoparticles in a hexagonal arrangement and found an increase in resonance linewidth with increasing spacing. Apart from the influence of the domain size we also expect the multidomain character of the samples to contribute to the resonance broadening at large lattice constants. The multidomain character and the resulting large number of grain boundaries dampens the diffractive modes. In addition, there will be significant scattering losses at the domain boundaries as observed for guided resonances in 2D photonic crystals.[55]

To further support our experimental findings we performed FDTD simulations of lattices with finite sizes. Figure 5 d) shows the calculated spectra using the same lattice parameters as in the experiment and a domain size of four corresponding to 61 particles. Again, the simulated spectra have been normalized to 10 particles per μm^2. All peak positions as well as the experimental and simulated values of the resonance FWHM are presented in table 2. We find a very good match between experiment and simulation for all the different monolayers investigated, despite a small deviation in the SLR position that can be explained in terms of a small amount of positional disorder in the self-assembled lattices. This is in agreement

with the study of Auguié and Barnes.[56] Those authors found a blue shift in the SLR for increasing disorder.

In addition to far-field extinction spectra, we have also recorded local transmission spectra using a light microscope. Resulting spectra for the monolayer samples with d_{c-c} = 449 nm and d_{c-c} = 573 nm in asymmetric and symmetric RI environments are shown in the Supporting Information (Figure S7). The local spectra resemble the spectra collected using standard extinction spectroscopy. For the symmetric RI environment we observe SLRs for both lattice constants, while the d_{c-c} = 573 nm sample exhibitd a pronounced plasmonic contribution that almost matches the expected single particle LSPR, as well as the non-coupling case in an asymmetric RI environment.

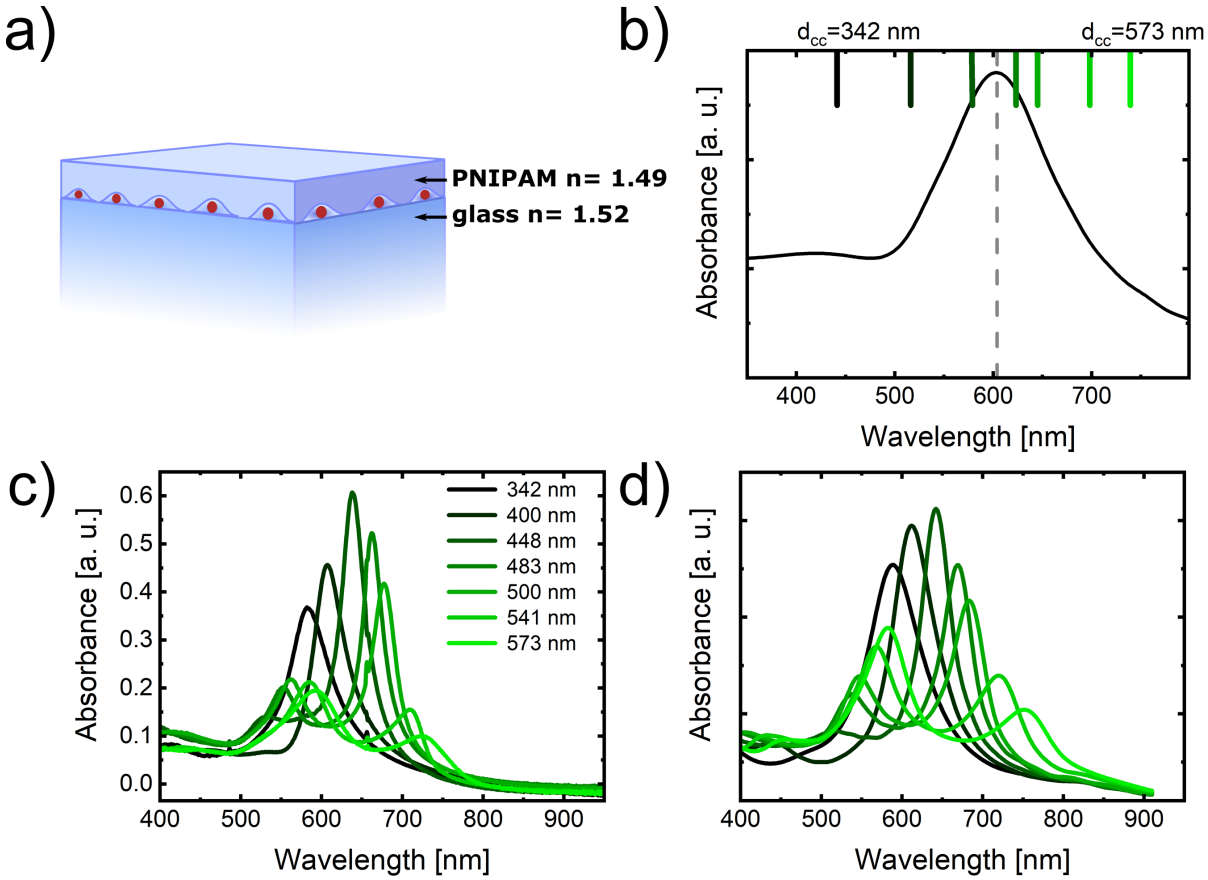

Figure 5: Optical properties of particle arrays in symmetric RI environment. a) Schematic figure of PNIPAM coated gold particle monolayer on glass substrate. b) calculated LSPR of single gold particle on glass substrate coated with 300 nm PNIPAM film with theoretical Bragg position for each interparticle distance. c) Absorbance with varying interparticle distance. d) FDTD simulated absorbance spectra of particle lattices (domain size 4) with varying spacing in homogeneous RI environment. The colour code in b), c) and d) refers to the same d_{c-c}. All spectra were normalized to account for the same number of particles per area (10 particles per μm^2).

Table 2: Calculated wavelength of the $\{1,0\}$ diffraction peak, λ_{Bragg}, resonance positions, λ_{max}, and FWHM values for lattices with various d_{c-c} for both asymmetric and symmetric RI environments. Values in brackets correspond to results from FDTD simulations.

d_{c-c} [nm]	λ_{Bragg} [nm]	λ_{max} [nm]		FWHM [nm]	
		asymmetric	symmetric	asymmetric	symmetric
342 ± 44	441	561 (572)	583 (588)	78 (90)	75 (84)
400 ± 52	516	569 (578)	607 (612)	71 (77)	52 (65)
448 ± 60	578	585 (590)	638 (642)	69 (79)	40 (47)
483 ± 46	623	592 (596)	662 (670)	106 (103)	33 (50)
500 ± 51	645	593 (596)	678 (684)	127 (111)	42 (61)
541 ± 30	698	595 (596)	710 (718)	136 (121)	67 (107)
573 ± 42	739	595 (596)	726 (750)	145 (127)	124 (132)

Direct comparisons of asymmetric and symmetric RI environments

We now want to directly compare and discuss the differences in optical response in asymmetric and symmetric RI environments. In order to be comparable to other studies in the literature and to other lattice symmetries, we will use the lattice period instead of d_{c-c} in the following discussions. Figure 6 a) shows extinction cross-sections obtained from FDTD simulations for hexagonal infinite lattices of spherical AuNPs (100 nm in diameter) for various lattice periods in 10 nm steps. A constant RI = 1.49 for the PNIPAM topcoating as superstrate and RI = 1.52 for the glass substrate were used (symmetric environment) which match closely the expected RIs from the experiment. With increasing period, the resonance maximum continuously shifts to the red while the linewidths become smaller. For large periods the resonance positions asymptotically approach the $(0, \pm 1)$ RA (solid line) implying that the resonance character becomes more and more photonic and less plasmonic. Figure 6 b) compares electromagnetic near-field intensities calculated at the respective resonance wavelength, λ_{max} for the asymmetric (top row) and symmetric (bottom row) RI cases for three selected lattice periods. All maps reveal the excitation of dipolar resonances with stronger field strengths for the symmetric RI case caused by the higher effective average RI. In addition to the dipole excitation, the symmetric RI cases with periods of 388 nm (d_{c-c} = 448 nm) and 418 nm (d_{c-c} = 483 nm) that are labelled with α and β show the

typical in-plane diffractive band structure. The diffractive-plasmonic coupling in these two samples results in the formation of SLRs. From all resonances, the SLRs feature the highest field intensities. In experiment, we observe very similar results. Figure 6 c) shows the resonance wavelength, λ_{max}, determined for monolayer samples with different lattice periods in symmetric and asymmetric RI environment. For the symmetric case λ_{max} increases continuously with increasing period and asymptotically approaches the $(0, \pm 1)$ RA (red solid line) for the higher periods. These resonances correspond to SLRs for periods of 388 nm and larger (full circles). For smaller periods, the values of λ_{max} are close to the uncoupled LSPR (red horizontal bar) while showing a weak blueshift for decreasing periods. This blueshift is also observed in the asymmetric RI samples for periods in a very similar range (below approximately 400 nm).

For larger periods, λ_{max} approaches the uncoupled LSPR (grey horizontal bar) indicating that diffractive coupling is not supported due to the strong RI mismatch between substrate and superstrate in the asymmetric samples. The blueshift observed for decreasing periods is attributed to long-range dipolar interactions. We now want to focus on the SLRs observed in the symmetric RI samples and use the Q-factor to discuss the coupling strength in our self-assembled monolayers. Figure 6 d) compares the resonance position and Q-factor for the symmetric RI samples as a function of the spectral difference between the diffractive mode and the single particle LSPR, $\Delta\lambda = \lambda_{RA} - \lambda_{LSPR}$. Both λ_{max} and the Q-factor decrease in a nearly linear manner for decreasing $\Delta\lambda$ below -50 nm. In this region diffractive-plasmonic coupling is inhibited and only long-range dipolar interactions become relevant. For values of $\Delta\lambda$ approaching 0 and larger where SLRs appear, the resonance shift becomes steeper and the Q-factor increases significantly reaching a maximum for $\Delta\lambda \approx 20$ nm corresponding to a period of 418 nm. Here the Q-factor reaches a value of approximately 20.

For further increases in $\Delta\lambda$, the Q-factor decreases significantly indicating increasing losses. This decrease is contrary to the observation from simulation in Figure 6 a) and studies reported in literature where an increase in Q-factor is observed due to the increasing

photonic character and reducing plasmonic losses for larger periods. We attribute our findings to the finite domain size in our lattices and scattering losses from domain boundaries and lattice defects. To support this we compare the resonance FWHM for various domain sizes as a function of lattice period from FDTD simulation in Figure 6 e). For domain sizes of two to five, we observe an increase in FWHM with increasing period while for each period the FWHM is larger the smaller the period. In other words, the resonance linewidth increases and thus the Q-factor decreases with decreasing domain size and increasing period. The respective representation of the Q-factor can be found in the Supporting Information (Figure S8). In contrast, the simulation using periodic boundary conditions (and thus resembling an infinite lattice) reveals a decrease in FWHM with increasing period and an increase in Q-factor. Similar effects of the array size on the Q-factor of the SLR were found by Rodriguez *et al.*[27]

To summarize, there are pronounced differences in the behaviour of SLRs in asymmetric and symmetric RI samples. We find: 1) A close match between the RI of the substrate and superstrate is required to enable plasmonic coupling with in-plane modes of diffraction. 2) SLRs are only supported for diffraction wavelengths close to, or larger than, the single particle LSPR wavelength. 3) For diffraction wavelengths significantly smaller than the LSPR wavelength, long-range dipolar interactions are observed, leading to a blueshift with decreasing lattice period. 4) High Q-factor SLRs are observed for slightly longer wavelengths of diffraction compared to the LSPR, whereas a reduction in Q-factor is observed for larger offsets of diffraction and LSPR wavelengths. The latter reduction in Q-factor is caused by finite domain size effects and scattering losses.

Despite the obvious influence of lattice imperfections in our self-assembled lattices, the maximum Q-factor of $Q \approx 20$ for a period of 418 nm is more than half of the value obtained from FDTD simulation for an infinite lattice using periodic boundary conditions ($Q \approx 37$, see Figure S9 in the Supporting Information). Similar calculated results were obtained by

Rodriguez *et al.*[27] for square arrays of gold discs with 120 nm diameter and 50 nm height. For an infinite array they calculated $Q \approx 30$ and finite arrays with a few hundreds of particles already closely approached this limit.

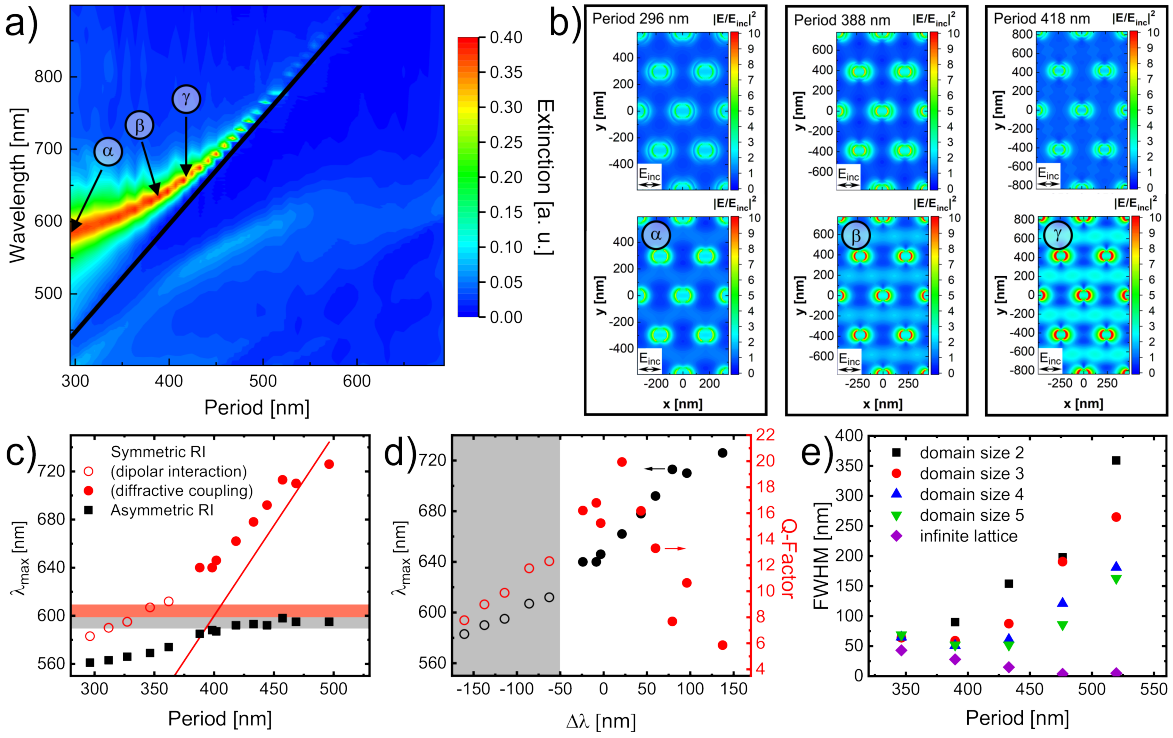

Figure 6: Comparison of different electromagnetic coupling regimes. a) Calculated extinction cross-sections for hexagonal arrays of gold spheres (100 nm diameter) for lattice periods in 10 nm steps and a symmetric environment with RI = 1.49 for the PNIPAM topcoating and RI = 1.52 for the glass substrate. The solid line corresponds to the (0,±1) Rayleigh anomaly (RA). b) Near-field electromagnetic intensity maps ($|E/E_{inc}^2|$) from FDTD simulations for heaxagonal monolayer with asymmetric RI (top row) and symmetric RI environment (bottom row). Calculations were performed at the respective λ_{max} of the samples. Corresponding spectral positions for the symmetric case labelled with α, β and γ are also indicated by arrows in a). c) Peak wavelength, λ_{max}, as a function of lattice period from experiment. Black squares: Asymmetric RI. Red circles: Symmetric RI. Filled red circles correspond to samples where diffractive-plasmonic coupling (SLRs) were observed. The red line corresponds to the (0,±1) RA. The light red and grey bars mark the LSPR position (no coupling) in symmetric and asymmetric RI, respectively. d) Experimental peak wavelength, λ_{max}, and Q-Factor as a function of wavelength difference between LSPR and RA, $\Delta\lambda = \lambda_{RA} - \lambda_{LSPR}$. e) FWHM of resonance peaks from FDTD simulations of hexagonal lattices in symmetric environment (RI = 1.49 for PNIPAM topcoating, RI = 1.52 for glass substrate) for different domain sizes. (The associated absorbance spectra from c) and d) are shown in Supporting Information S5)

Conclusions

We have experimentally and theoretically studied the optical properties of periodic gold nanoparticle arrays prepared via interface-mediated self-assembly. While weak electromagnetic coupling related to long-range radiative coupling of the dipoles was observed in strongly asymmetric refractive index environments, homogenization of the refractive index resulted in pronounced surface lattice resonances. In both cases, the coupling strength strongly depends on the interparticle distance. Radiative dipolar interactions increase with decreasing interparticle distance resulting in a blue-shift of the plasmon resonance. In contrast diffractive-plasmonic coupling becomes pronounced for larger distances where the in-plane modes of diffraction are spectrally close to, or redshifted from, the single particle, localized surface plasmon resonance. The spectral overlap between both modes weakens at large enough distances, and then the surface lattice resonances also become weaker in intensity and significantly broaden as a result of the finite size of the crystalline domains in the sample. As a consequence of the decreasing coupling efficiency at increasing lattice constants, the purely plasmonic contribution at lower wavelengths reappears due to energy conservation. Although our experimental samples feature lattice defects and limited single crystalline domain sizes, the deviation of the experimentally observed surface lattice resonance width and intensity from simulations of infinite size lattices is small. This implies that colloidal self-assembly is competitive compared to lithographic approaches commonly applied for the preparation of near-perfect periodic plasmonic lattices. We believe that particle arrays supporting much higher quality factor resonances are readily achievable by self-assembly, because the individual plasmonic particle sizes, shapes and interparticle spacing can all be adjusted.

Our work significantly contributes to a deeper understanding of electromagnetic coupling phenomena in periodic plasmonic arrays. Furthermore we demonstrate the enormous potential of colloidal self-assembly for the fabrication of cm^2-scale samples with tailored plasmonic properties based on relatively simple colloidal building blocks. In future work we will address the possiblity for further improvement of the quality factor of surface lattice resonances by

optimization of the plasmonic colloidal building blocks and the lattice geometry.

Acknowledgements

The authors acknowledge financial support by the German Academic Exchange service (DAAD) through its Thematic Network Melbourne-Bayreuth Polymer/Colloid Network sponsored from funds of the Federal Ministry of Education and Research (BMBF). PM thanks the ARC for support through Grant CE170100026. MK acknowledges the German Research Foundation (DFG) for funding under grant KA3880/6-1. The authors thank Heyou Zhang from the University of Melbourne for his assistance with the DFM measurements and Sophia Köhler from the Heinrich-Heine-University Düsseldorf for her assistance with the TEM measurements.

References

(1) Maier, S. A.; Brongersma, M. L.; Kik, P. G.; Meltzer, S.; Requicha, A. a. G.; Atwater, H. A. Plasmonics–A Route to Nanoscale Optical Devices. *Advanced Materials* **2001**, *13*, 1501–1505.

(2) Rodríguez-González, B.; Burrows, A.; Watanabe, M.; Kiely, C. J.; Marzán, L. M. L. Multishell bimetallic AuAg nanoparticles: synthesis, structure and optical properties. *Journal of Materials Chemistry* **2005**, *15*, 1755.

(3) Kelly, K. L.; Coronado, E.; Zhao, L. L.; Schatz, G. C. The Optical Properties of Metal Nanoparticles: The Influence of Size, Shape and Dielectric Environment. *The Journal of Physical Chemistry B* **2003**, *107*, 668–677.

(4) Rodríguez-Fernández, J.; Pérez-Juste, J.; de Abajo, F. J. G.; Liz-Marzán, L. M. Seeded Growth of Submicron Au Colloids with Quadrupole Plasmon Resonance Modes. *Langmuir* **2006**, *22*, 7007–7010.

(5) Mock, J. J.; Barbic, M.; Smith, D. R.; Schultz, D. A.; Schultz, S. Shape effects in plasmon resonance of individual colloidal silver nanoparticles. *The Journal of Chemical Physics* **2002**, *116*, 6755–6759.

(6) Nehl, C. L.; Hafner, J. H. Shape-dependent plasmon resonances of gold nanoparticles. *Journal of Materials Chemistry* **2008**, *18*, 2415.

(7) Mulvaney, P. Surface Plasmon Spectroscopy of Nanosized Metal Particles. *Langmuir* **1996**, *12*, 788–800.

(8) Kasani, S.; Curtin, K.; Wu, N. A review of 2D and 3D plasmonic nanostructure array patterns: fabrication, light management and sensing applications. *Nanophotonics* **2019**, *8*, 2065–2089.

(9) Wang, W.; Ramezani, M.; Väkeväinen, A. I.; Törmä, P.; Rivas, J. G.; Odom, T. W. The rich photonic world of plasmonic nanoparticle arrays. *Materials Today* **2018**, *21*, 303–314.

(10) Fitzgerald, J. P. S.; Karg, M. Plasmon resonance coupling phenomena in self-assembled colloidal monolayers. *Physica Status Solidi A* **2017**, *214*, 1600947.

(11) Funston, A. M.; Gómez, D. E.; Karg, M.; Vernon, K. C.; Davis, T. J.; Mulvaney, P. Aligned Linear Arrays of Crystalline Nanoparticles. *The Journal of Physical Chemistry Letters* **2013**, *4*, 1994–2001.

(12) Mayer, M.; Potapov, P. L.; Pohl, D.; Steiner, A. M.; Schultz, J.; Rellinghaus, B.; Lubk, A.; König, T. A. F.; Fery, A. Direct Observation of Plasmon Band Formation and Delocalization in Quasi-Infinite Nanoparticle Chains. *Nano Letters* **2019**, *19*, 3854–3862.

(13) Maier, S. A.; Kik, P. G.; Atwater, H. A.; Meltzer, S.; Harel, E.; Koel, B. E.; Re-

quicha, A. A. Local detection of electromagnetic energy transport below the diffraction limit in metal nanoparticle plasmon waveguides. *Nature Materials* **2003**, *2*, 229–232.

(14) Bastús, N. G.; Merkoçi, F.; Piella, J.; Puntes, V. Synthesis of Highly Monodisperse Citrate-Stabilized Silver Nanoparticles of up to 200 nm: Kinetic Control and Catalytic Properties. *Chemistry of Materials* **2014**, *26*, 2836–2846.

(15) Jain, P. K.; Huang, X.; El-Sayed, I. H.; El-Sayed, M. A. Review of Some Interesting Surface Plasmon Resonance-enhanced Properties of Noble Metal Nanoparticles and Their Applications to Biosystems. *Plasmonics* **2007**, *2*, 107–118.

(16) Giannini, V.; Fernández-Domínguez, A. I.; Heck, S. C.; Maier, S. A. Plasmonic Nanoantennas: Fundamentals and Their Use in Controlling the Radiative Properties of Nanoemitters. *Chemical Reviews* **2011**, *111*, 3888–3912.

(17) Atwater, H. A.; Polman, A. Erratum: Plasmonics for improved photovoltaic devices. *Nature Materials* **2010**, *9*, 865–865.

(18) Singh, C. R.; Honold, T.; Gujar, T. P.; Retsch, M.; Fery, A.; Karg, M.; Thelakkat, M. The role of colloidal plasmonic nanostructures in organic solar cells. *Physical Chemistry Chemical Physics* **2016**, *18*, 23155–23163.

(19) Willets, K. A.; Van Duyne, R. P. Localized surface plasmon resonance spectroscopy and sensing. *Annual Review of Physical Chemistry* **2007**, *58*, 267–297.

(20) Noginov, M. A.; Zhu, G.; Belgrave, A. M.; Bakker, R.; Shalaev, V. M.; Narimanov, E. E.; Stout, S.; Herz, E.; Suteewong, T.; Wiesner, U. Demonstration of a spaser-based nanolaser. *Nature* **2009**, *460*, 1110–1112.

(21) Ueno, K.; Misawa, H. Surface plasmon-enhanced photochemical reactions. *Journal of Photochemistry and Photobiology C: Photochemistry Reviews* **2013**, *15*, 31–52.

(22) Sönnichsen, C.; Franzl, T.; Wilk, T.; von Plessen, G.; Feldmann, J.; Wilson, O.; Mulvaney, P. Drastic Reduction of Plasmon Damping in Gold Nanorods. *Physical Review Letters* **2002**, *88*, 077402.

(23) West, P. R.; Ishii, S.; Naik, G. V.; Emani, N. K.; Shalaev, V. M.; Boltasseva, A. Searching for better plasmonic materials. *Laser & Photonics Reviews* **2010**, *4*, 795–808.

(24) Kravets, V. G.; Kabashin, A. V.; Barnes, W. L.; Grigorenko, A. N. Plasmonic Surface Lattice Resonances: A Review of Properties and Applications. *Chemical Reviews* **2018**, *118*, 5912–5951.

(25) Bastús, N. G.; Comenge, J.; Puntes, V. Kinetically Controlled Seeded Growth Synthesis of Citrate-Stabilized Gold Nanoparticles of up to 200 nm: Size Focusing versus Ostwald Ripening. *Langmuir* **2011**, *27*, 11098–11105.

(26) Zhou, W.; Dridi, M.; Suh, J. Y.; Kim, C. H.; Co, D. T.; Wasielewski, M. R.; Schatz, G. C.; Odom, T. W. Lasing action in strongly coupled plasmonic nanocavity arrays. *Nature Nanotechnology; London* **2013**, *8*, 506–11.

(27) Rodriguez, S. R. K.; Schaafsma, M. C.; Berrier, A.; Gómez Rivas, J. Collective resonances in plasmonic crystals: Size matters. *Physica B: Condensed Matter* **2012**, *407*, 4081–4085.

(28) Ross, M. B.; Mirkin, C. A.; Schatz, G. C. Optical Properties of One-, Two-, and Three-Dimensional Arrays of Plasmonic Nanostructures. *The Journal of Physical Chemistry C* **2016**, *120*, 816–830.

(29) Kravets, V. G.; Schedin, F.; Grigorenko, A. N. Extremely Narrow Plasmon Resonances Based on Diffraction Coupling of Localized Plasmons in Arrays of Metallic Nanoparticles. *Physical Review Letters* **2008**, *101*, 087403.

(30) Auguié, B.; Barnes, W. L. Collective Resonances in Gold Nanoparticle Arrays. *Physical Review Letters* **2008**, *101*, 143902.

(31) Cherqui, C.; Bourgeois, M. R.; Wang, D.; Schatz, G. C. Plasmonic Surface Lattice Resonances: Theory and Computation. *Accounts of Chemical Research* **2019**, *52*, 2548–2558.

(32) Humphrey, A. D.; Barnes, W. L. Plasmonic surface lattice resonances on arrays of different lattice symmetry. *Physical Review B* **2014**, *90*, 075404.

(33) Humphrey, A. D.; Meinzer, N.; Starkey, T. A.; Barnes, W. L. Surface Lattice Resonances in Plasmonic Arrays of Asymmetric Disc Dimers. *ACS Photonics* **2016**, *3*, 634–639.

(34) Henzie, J.; Lee, M. H.; Odom, T. W. Multiscale patterning of plasmonic metamaterials. *Nature Nanotechnology* **2007**, *2*, 549–554.

(35) Honold, T.; Volk, K.; Rauh, A.; Fitzgerald, J. P. S.; Karg, M. Tunable plasmonic surfaces via colloid assembly. *Journal of Materials Chemistry C* **2015**, *3*, 11449–11457.

(36) Volk, K.; Fitzgerald, J. P. S.; Retsch, M.; Karg, M. Time-Controlled Colloidal Superstructures: Long-Range Plasmon Resonance Coupling in Particle Monolayers. *Advanced Materials* **2015**, *27*, 7332–7337.

(37) Honold, T.; Volk, K.; Retsch, M.; Karg, M. Binary plasmonic honeycomb structures: High-resolution EDX mapping and optical properties. *Colloids and Surfaces A: Physicochemical and Engineering Aspects* **2016**, *510*, 198–204.

(38) Volk, K.; Fitzgerald, J. P. S.; Ruckdeschel, P.; Retsch, M.; König, T. A. F.; Karg, M. Reversible Tuning of Visible Wavelength Surface Lattice Resonances in Self-Assembled Hybrid Monolayers. *Advanced Optical Materials* **2017**, *5*, 1600971.

(39) Volk, K.; Fitzgerald, J. P. S.; Karg, M. In-Plane Surface Lattice and Higher Order Resonances in Self-Assembled Plasmonic Monolayers: From Substrate-Supported to Free-Standing Thin Films. *ACS Applied Materials & Interfaces* **2019**, *11*, 16096–16106.

(40) Chu, Y.; Schonbrun, E.; Yang, T.; Crozier, K. B. Experimental observation of narrow surface plasmon resonances in gold nanoparticle arrays. *Applied Physics Letters* **2008**, *93*, 181108.

(41) Turkevich, J.; Stevenson, P. C.; Hillier, J. A study of the nucleation and growth processes in the synthesis of colloidal gold. *Discussions of the Faraday Society* **1951**, *11*, 55–75.

(42) Rauh, A.; Honold, T.; Karg, M. Seeded precipitation polymerization for the synthesis of gold-hydrogel core-shell particles: the role of surface functionalization and seed concentration. *Colloid and Polymer Science* **2016**, *294*, 37–47.

(43) Ebeling, B.; Vana, P. RAFT-Polymers with Single and Multiple Trithiocarbonate Groups as Uniform Gold-Nanoparticle Coatings. *Macromolecules* **2013**, *46*, 4862–4871.

(44) Schneider, C. A.; Rasband, W. S.; Eliceiri, K. W. NIH Image to ImageJ: 25 years of image analysis. *Nature Methods* **2012**, *9*, 671–675.

(45) Johnson, P. B.; Christy, R. W. Optical Constants of the Noble Metals. *Physical Review B* **1972**, *6*, 4370–4379.

(46) Müller, M. B.; Kuttner, C.; König, T. A. F.; Tsukruk, V. V.; Förster, S.; Karg, M.; Fery, A. Plasmonic Library Based on Substrate-Supported Gradiential Plasmonic Arrays. *ACS Nano* **2014**, *8*, 9410–9421.

(47) Reufer, M.; Dıaz-Leyva, P.; Lynch, I.; Scheffold, F. Temperature-sensitive poly(N-Isopropyl-Acrylamide) microgel particles: A light scattering study. *The European Physical Journal E* **2009**, *28*, 165–171.

(48) Hillebrand, R.; Müller, F.; Schwirn, K.; Lee, W.; Steinhart, M. Quantitative Analysis of the Grain Morphology in Self-Assembled Hexagonal Lattices. *ACS Nano* **2008**, *2*, 913–920.

(49) Haynes, C. L.; McFarland, A. D.; Zhao, L.; Van Duyne, R. P.; Schatz, G. C.; Gunnarsson, L.; Prikulis, J.; Kasemo, B.; Käll, M. Nanoparticle Optics: The Importance of Radiative Dipole Coupling in Two-Dimensional Nanopartile Arrays. *The Journal of Physical Chemistry B* **2003**, *107*, 7337–7342.

(50) Jenkins, J. A.; Zhou, Y.; Thota, S.; Tian, X.; Zhao, X.; Zou, S.; Zhao, J. Blue-Shifted Narrow Localized Surface Plasmon Resonance from Dipole Coupling in Gold Nanoparticle Random Arrays. *The Journal of Physical Chemistry C* **2014**, *118*, 26276–26283.

(51) Ghosh, S. K.; Pal, T. Interparticle Coupling Effect on the Surface Plasmon Resonance of Gold Nanoparticles: From Theory to Applications. *Chemical Reviews* **2007**, *107*, 4797–4862.

(52) Yang, A.; Li, Z.; Knudson, M. P.; Hryn, A. J.; Wang, W.; Aydin, K.; Odom, T. W. Unidirectional Lasing from Template-Stripped Two-Dimensional Plasmonic Crystals. *ACS Nano* **2015**, *9*, 11582–11588.

(53) Wang, D.; Yang, A.; Hryn, A. J.; Schatz, G. C.; Odom, T. W. Superlattice Plasmons in Hierarchical Au Nanoparticle Arrays. *ACS Photonics* **2015**, *2*, 1789–1794.

(54) Zou, S.; Janel, N.; Schatz, G. C. Silver nanoparticle array structures that produce remarkably narrow plasmon lineshapes. *The Journal of Chemical Physics* **2004**, *120*, 10871–10875.

(55) Grepstad, J. O.; Greve, M. M.; Holst, B.; Johansen, I.-R.; Solgaard, O.; Sudbø, A. Finite-size limitations on Quality Factor of guided resonance modes in 2D Photonic Crystals. *Optics Express* **2013**, *21*, 23640–23654.

(56) Auguié, B.; Barnes, W. L. Diffractive coupling in gold nanoparticle arrays and the effect of disorder. *Optics Letters* **2009**, *34*, 401–403.

TOC

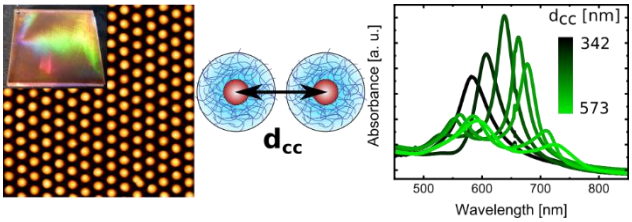
d_{cc}
d_{cc} [nm]
342
573
Absorbance [a. u.]
500
600
700
800
Wavelength [nm]